Pump it up: bioelectric stimulation controls tissue hydrostatic pressure and water transport via electro-inflation

Gawoon Shim[1, 5], **Isaac B. Breinyn**[2, 5], **Alejandro Martínez-Calvo**[3, 4, 5], **and Daniel J. Cohen**[1,✉]

[1]Department of Mechanical and Aerospace Engineering, Princeton University, Princeton, NJ 08540 USA
[2]Department of Quantitative and Computational Biology, Princeton University, Princeton, NJ 08540 USA
[3]Department of Chemical and Biological Engineering, Princeton University, Princeton, NJ 08540 USA
[4]Princeton Center for Theoretical Science, Princeton University, Princeton, NJ 08540 USA
[5]These authors contributed equally to this work.

Epithelial tissues sheath many organs, separating 'outside' from 'inside' and exquisitely regulating ion and water transport via electromechanical pumping to maintain homeostatic balance and tissue hydrostatic pressure. While it is becoming increasingly clear that the ionic microenvironment and external electric stimuli can affect epithelial function and behavior, the coupling between electrical perturbation and tissue form remain unclear. We investigated this by combining electrical stimulation with three-dimensional epithelial tissues with hollow 'lumens'—both kidney cysts and complex intestinal stem cell organoids. Our core finding is that physiological strength electrical stimulation of order 1-3 V/cm (with both direct and alternating currents) can drive powerful and rapid inflation of hollow tissues through a process we call 'electro-inflation', inducing a nearly threefold increase in tissue volume and striking asymmetries in tissue form. Electro-inflation is primarily driven by activation of the CFTR ion channel pumping chloride into the tissue, causing water to osmotically flow. This influx generates hydrostatic pressure, and inflation results from a competition between this pressure and cell cytoskeletal tension. We validated these interpretations with computational models connecting ion dynamics in the Diffuse Double Layer around tissues to tissue mechanics. Electro-inflation is a unique biophysical process to study and control complex tissue function.

epithelia | bioelectric stimulation | hydrostatic pressure | ion pumping | multicellularity

Correspondence: ***danielcohen@princeton.edu***

Introduction

Epithelia—sheet-like multicellular tissues with strong cell-cell adhesion—are foundational to animal life (1) as they can separate 'outside' from 'inside' by self-assembling into 3D, lumenized (hollow) structures such as tubules (e.g. kidney ducts), intricately folded surfaces (gut epithelium, choroid plexus), and hollow cysts (e.g. lung alveoli, organoids) (2). Epithelia are intrinsically electromechanical structures and play three critical, interlinked roles in lumenized structures to maintain homeostasis (3): (1) regulation of endogenous ionic currents via ion transport (4, 5); (2) regulation of water transport and osmolarity in response to ion gradients (180 L/day in the kidney (6)); and (3) generation and support of hydrostatic pressure resulting from water transport, all of which can be experimentally measured (7–10). This electromechanical sequence of ions, water, and pressure generation is increasingly recognized as a key factor regulating morphogenesis in complex 3D systems such as cysts and branching intestinal organoids (7–9) by providing the system biomechanical cues for size control and morphology. Transport across the epithelial layer controls cellular proliferation, differentiation, and rearrangement through luminal depositions of ions and proteins that affect cellular signaling and coordination as well as build-up of hydrostatic pressure that affects cortical tension, tissue stiffness, and maturation of tight junctions in tissues (11). Given the broad importance of epithelia and their intrinsic electromechanical nature, we investigated how externally manipulating ionic currents affected the growth dynamics of 3D epithelial tissues.

Bioelectric manipulation of epithelia is rooted in the 19th c. discoveries of Matteuci (12) and du Bois (13) that damage to skin (a stratified epithelium) induces a transient 'wound current', which we now know both arises from local disruption of homeostatic ionic currents (14–16) and can occur in any disruptive process spanning healing, embryonic development, and disease progression (14, 15, 17–22). Crucially, cells sense and respond to these ionic currents through a variety of mechanisms including electrophoretic and electrokinetic displacement of membrane-bound receptors and activation of ion channels (15, 16, 23, 24). In 2D epithelia, responses to external electric fields include regulation of cell volume and homeostasis (25), transcriptional changes (16, 26), and 'electrotaxis' (galvanotaxis)—the directed migration of cells down ionic gradients (typ. 1 V/cm) (15, 27). In this case, 2D epithelia undergo particularly dramatic electrotactic collective migration (28–33) which can be precisely controlled by spatiotemporally varying the electric field to induce arbitrary maneuvers or accelerate scratch wound healing (14, 28, 34, 35). Here, we extend this work into 3D epithelial tissue models (hollow cysts and organoids) in an attempt to manipulate tissue morphology.

We used the MDCK kidney cell cyst as our initial model system for a luminal epithelial structures as MDCKs form single-layered, hollow cysts that are extremely well studied and known recapitulate key developmental processes including apicobasal polarization of cells, active ionic and water transport, strong cell-cell junctions, and control of cell growth and proliferation (2, 9, 36). To electrically stimulate

these cysts, we grew them within a hydrogel matrix (Geltrex or Matrigel) that we embedded within a modified version of our SCHEEPDOG electrobioreactor (29, 30, 34, 35) that allowed us to combine: live imaging; media perfusion for bioreactor culture; and closed-loop electrical stimulation over a range of electric field strengths. Given our prior epithelial electrotaxis data, we hypothesized that we would see strong, 3D electrotaxis, but we instead observed a novel response upon electrically stimulating these cysts. Rather than directional migration, the cysts dramatically and rapidly increased in volume, inflating continuously when we applied an electrical field and deflating upon removal of the field. We investigated this and found that the inflation rate varies directly with the magnitude of the electric field. This inflation is mechanically mediated by cortical tension, and we showed through the use of inhibitors that the actomyosin network mechanically stabilizes and constrains growth of the cyst, akin to a spherical pressure vessel. Next, we used ion channel inhibitors to reveal that chloride-specific ion transport channels (CFTR and NKCC) account for the majority of the inflation response. We developed a first-principles computational model for this inflation supporting the concept that external electric bias could ultimately drive increased water transport. Interestingly, an extension of this model predicted the asymmetric build-up of ionic species around a 3D tissue under an external electric field, and 3D imaging confirmed that these cysts were asymmetrically inflation. This asymmetry could be modulated by switching field polarity back and forth, suggesting plasticity to the underlying 3D tissue. Finally, we demonstrate that this 'electro-inflation' and CFTR-mediated response generalizes to other lumenized models such as intestinal organoids.

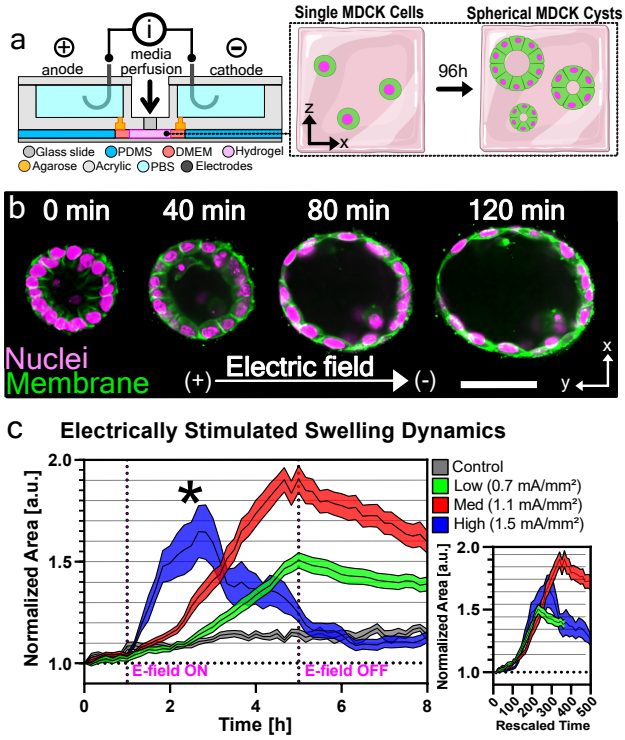

Fig. 1 | Electrical stimulation increases volume of lumenized epithelia. **a**, Cross-section of the electro-bioreactor. Inlay: Single MDCK cells form single-layered spherical cysts with hollow lumens after 96 hours of culture. **b**, Direct current electrical stimulation drives accelerated inflation in MDCK cysts. After 2 hours of stimulation, cysts approximately double in size. **c**, Inflation dynamics of cysts stimulated with low current (0.7 mA/mm^2, 1 V/cm), medium current (1.1 mA/mm^2, 2.25 V/cm) and high current (1.5 mA/mm^2, 3.5 V/cm), normalized to cyst area at $t = 0$ h. Stimulation begins at 1 h and ends at 5 h, as shown by the vertical dotted lines. The asterisk indicates cysts stimulated with high current exhibiting sudden rupture before stimulation is over, causing them to deflate before stimulation is over. Outlay: inflation curves collapse to a master curve after rescaling time using a power-law fit (see methods).

Results

Direct current electrical stimulation drives inflation in hollow epithelial cysts. To study how lumenized 3D structures respond to DC electrical stimulation, we stimulated MDCK epithelial cysts with a DC electrical field using a modified version of the SCHEEPDOG bioreactor (29, 34) containing two stimulation electrodes, electrochemical safeguards, perfusion lines, and a large, glass coverslide foundation to support high resolution 3D imaging during stimulation (Supplementary Fig. 1, Methods). Single MDCK cells were seeded into a basement membrane hydrogel (Geltrex) on top of the coverslip platform and cultured for 96 h as they self-assembled into spherical, lumenized structures approximately 50 μm in diameter (Fig. 1a). The resulting cysts typically had a single (or multiple, Supplementary Information) hollow lumen, occasionally containing debris from cells having undergone apoptosis during lumen development. Reported field strengths in vivo fields are $\mathcal{O}$(1 V/cm), but the current density is the key design parameter (15, 28, 37), so we used a current-controlled supply and fixed microfluidic bioreactor dimensions to deliver 0.7 mA/mm^2 to 1.5 mA/mm^2 (equivalent to 1V/cm to 4V/cm) to suspended tissues and validated stimulation uniformity using both finite element simulations (Supplementary Fig. 2) and real-time channel voltage monitoring. We observed dramatic changes upon stimulation, not via migration as expected, but via rapid volumetric inflation (a 2X increase in cross-section and nearly 3X increase in volume), as shown in 3D confocal sections in Fig. 1b and Supplementary Video 1. Closer examination revealed two distinct phenotypes: 1) overall increases in volume as the luminal space expands and 2) asymmetric deformation of the epithelium, with one side thickening while the other thins (Supplementary Video 2), and we proceeded to analyze each phenotype in turn.

To better understand the striking tissue volume change induced by electrical stimulation, we first characterized the broad dynamics of the inflation process and the relationship between input stimulation and output inflation by varying the input field strength over three levels: low (1V/cm; 0.7 mA/mm^2), medium (2.25 V/cm; 1.1 mA/mm^2), and high (3.5 V/cm; 1.5 mA/mm^2). All initial experiments were performed using time-lapse (10 min/frame), phase contrast imaging as follows: control observation for 1 h; electrical stimulation for 4 h; relaxation without the field for 3 h. Data were analyzed by segmenting the phase contrast images at each timepoint and calculating the cross-sectional area of the cysts at the spherical equator using a custom ImageJ script (Methods). The cross-sectional area for each individual cyst was normal-

ized to the value at $t = 0$ and filtered for artifacts (Supplementary Fig. 3). Each epithelial cyst originates from a single cell, meaning cysts are clonal and subject to any heterogeneity in the population. Cysts themselves also exhibit considerable heterogeneity in culture (36, 38).

To compensate for this heterogeneity and better capture the upper limit of what is possible, we directly compared the cross-sectional area dynamics for the top quartile of control and stimulated cysts in Fig. 1c (Supplementary Video 3; the complete set of all raw traces is shown in Supplementary Fig. 3). In all cases, cysts began to inflate within 20 minutes of electrical stimulation, exhibiting a clear and direct relation between the rate and extent of inflation and applied electrical field strength. In all cases, stimulated tissues exhibited a pronounced difference in inflation relative to unstimulated tissues (Fig. 1c, gray). In the strongest field case, inflation proceeded so rapidly that many cysts appeared to burst, likely from being over-pressurized (Fig. 1c, blue, '*'). These burst cysts are capable of repairing themselves but the majority cease inflation post-rupture. More generally, we found that peak inflation volumes appeared capped and could not be increased indefinitely with field strength or duration. In both types of inflation, with or without rupture, no cellular death was seen over the course of luminal inflation (Supplementary Video 4, 5). Prolonging the duration of electrical stimulation at medium current also did not inflate the system further (Supplementary Fig. 4). This suggests that there is a mechanical limit to how much pressure the cyst can withhold, possibly set by the cytoskeletal structure within the cyst, a hypothesis we explore in the subsequent section. Once electrical stimulation was removed, the cysts gradually decreased in volume until they converged on the volume of time-matched control cysts, surprisingly (Fig. 1c from 5+ hrs; Supplementary Fig. 5 for longer duration).

To explore the generality of the electro-inflation response, all inflation curves were rescaled using a power-law fit (see methods, Supp. Fig. 6), after which the data collapsed onto a single master curve (Fig. 1c, outlay). This shows that the kinetics of electro-inflation are self-similar across experimental conditions, and the mechanisms governing the response are conserved across stimulus strength. This is further shown by the independence of the cysts' relative change in cross-sectional area on their initial area (Supplementary Fig. 7), supporting the claim that this process is general and agnostic of the intrinsic properties of the cyst. Given this, we used a 'medium' electric field strength (1.1 mA/mm^2, 2.25 V/cm) for all further experiments, which we calculated corresponds to an inflation rate of approximately 2 nL/min if we assume cysts are spheres and generalize from the equatorial cross-section changes plotted in Fig. 1.

Traditionally, inflation is induced and studied in lumenized structures by using pharmaceutical agents targeting ion channels (39–42) and osmotic flow (43). Here we evaluated the effect of the commonly used drug forskolin, which acts by elevating cyclic AMP (cAMP) levels to trigger downstream protein kinase A (PKA) and the apical chloride channel 'chloride channel cystic fibrosis transmembrane conductance regulator' (CFTR) (Supplementary Fig. 8) (44, 45).Interestingly, we found that electrically mediated inflation far outstrips forskolin-induced inflation over the experimental duration, with forskolin reported to primarily drive inflation over a multi-day period (46). Overall, these findings suggest that electrical stimulation activates a powerful and reversible inflation mechanism in the epithelial cysts, raising the question of how this is regulated.

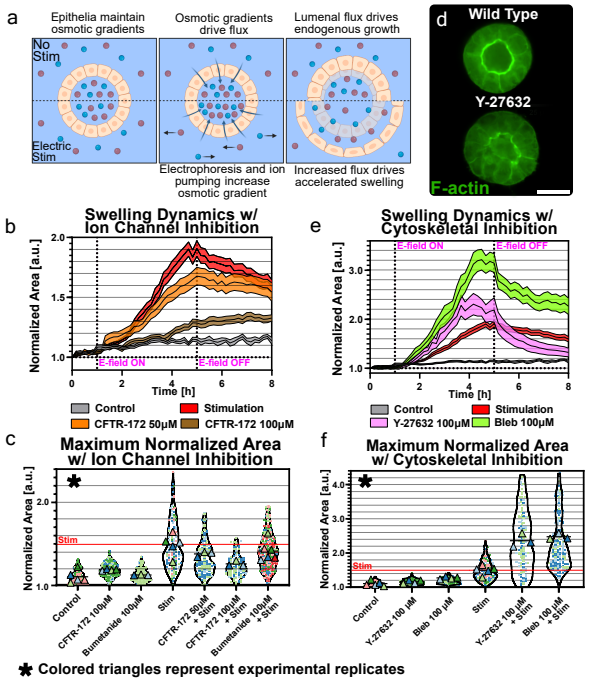

Fig. 2 | Ion pumping and cytoskeletal mechanics mediate electrical stimulation-mediated inflation. **a**, Schematic of the process by which MDCK cysts endogenously inflate, and how the inflation mechanism is modulated by electrical stimulation. **b**, Inflation dynamics averaged for the top quartile of cysts treated with different concentrations of CFTR-172, an inhibitor of the cystic fibrosis transmembrane conductance Regulator (CFTR) chloride channel. **c**, SuperPlot of the maximum normalized area of all cysts treated with apicobasal ion channel inhibitors, with and without electrical stimulation. **d**, (Top) Equatorial confocal slice of a cyst stained for F-actin, showing the actomyosin cortex that makes up the apical domain of the structure. (Bottom) a cyst that has been treated with Y-27632, a ROCK inhibitor, with an improperly structured lumen. **e**, Inflation dynamics averaged for the top quartile of cysts treated with Y-27632 (ROCK inhibitor), and blebbistatin (myosin inhibitor). **f**, SuperPlot of the maximum normalized area of all cysts treated with cytoskeletal-related inhibitors, with and without electrical stimulation.

Electrically-actuated ion channels and water flow drive tissue inflation. We next investigated how electrical stimulation facilitates inflation in epithelial cysts. As electrically-induced inflation happens on the timescale of several hours, we ruled out the possibility that proliferation is the major drive behind the initial volume increase, although it may play a role in the long-term relaxation dynamics where we observed a bimodal response where some cysts remain significantly inflated while others gradually collapsed (Supplementary Fig. 5). Hence, we hypothesized that there are two possible mechanisms for electrical inflation: (1) direct actuation of water pumping into the lumen through aquaporins or paracellular fluid flow; or (2) actuation of ion pumping, which would drive osmotic gradients and subsequent water pumping. We focused on this second mechanism both as the

build-up of osmotic gradients across the epithelia is known to drive water transport and lumen growth (7–9), and as DC electric fields will naturally affect ion distribution in fluid and create osmotic gradients across micro-structures (Fig. 2a) (39, 47, 48).

Inhibiting apical and basal ion channels allowed us to test if field-induced ion transport regulated cyst inflation. We focused on chloride transporters as chloride ion secretion into the lumen is known as a key contributor to inflation of lumenized structures. The accepted mechanism contains two stages. First, chloride ion influx makes the lumen more negative, which triggers electrically-driven influx of sodium ions (positive) to balance the charge. Second, this net influx of salt ions into the lumen creates a strong osmotic gradient that drives water into the lumen via both paracellular and transcellular routes (49–51). Fig. 2a presents a cartoon of what this process might look like in the case of electro-inflating cysts (44) where the apical and basal surfaces might both contribute to ion flow. We aimed to inhibit both chloride influx into the lumen (targeting apical ion channels) and any chloride influx into the cell body itself (targeting basal ion channels).

For the apical chloride channel, we targeted cystic fibrosis transmembrane conductance regulator (CFTR) as its critical role in endogenous and chemical-induced inflation of MDCK cysts and other epithelial lumenized structures is well established (9, 44, 50). To test its role in transducing electrical stimulation into inflation, we inhibited CFTR using the CFTR-specific inhibitor CFTR-172 and investigated how it affected the inflation response (44, 52). Indeed, inhibiting CFTR dramatically reduced field-mediated inflation, suggesting that CFTR, or more generally, chloride transport, can account for perhaps 2/3 of the electro-inflation effect in the strongest inflaters (Fig. 2b). To achieve a noticeable effect, we tested two concentrations of the inhibitor (50/100 μM), both higher than what is required for unstimulated MDCK cysts, suggesting that electrical stimulation markedly increases CFTR activity well beyond the endogenous level for these tissues (9). We do note that CFTR-172 can potentially affect volume-sensitive outwardly rectifying chloride channels (VSOR) in murine renal distal convoluted tubules (DCT) or proximal convoluted tubules (PCT), so it is also possible that CFTR-172 could be inhibiting additional chloride channels beyond CFTR in our MDCK cysts (53). We further tested basal chloride transport by targeting the charge-balanced Na-K-Cl cotransporter (NKCC) with the inhibitor bumetanide and also saw significant reduction in the electro-inflation response. These inhibitor data are presented in 'SuperPlot' format (54) in Fig. 2c and all statistical tests are presented in Supplementary Fig. 9. Overall, these data demonstrate that electro-inflation is strongly mediated by chloride transport into the lumen via apical chloride transporters that lead to osmotic water transport and hydrostatic pressure changes.

Does the direction of fluid transport depend on which surface of the cyst–inside or outside–is electrically stimulated? To explore this, we electrically stimulated MDCK domes grown on a 2D substrate (55), a well-documented pseudo-3D model system. MDCK domes are inverted lumenal structure with an inward-facing basal membrane (opposite that of our cysts), meaning that electrical stimulation of dome cultures would directly stimulate the apical, rather than basal, surface. If the fluid pumping direction depended on which surface was stimulated, these inverted structures would also inflate when electrically stimulated because they would now pump fluid apical-to-basal and into these inverted cavities. Interestingly, stimulation of inverted tissues still induced a collapse and deflation of the domes (Supplementary Video 6). Once stimulation stopped, the domes re-inflated as fluid re-accumulated on the basal side of the membrane. Hence, electrical stimulation appears to induce basal-to-apical pumping independent of where on the tissue the stimulation is delivered.

Cystokeletal mechanics constrain inflation. There is clearly a mechanical component to electrically-induced tissue inflation, and the situation is akin to a spherical pressure vessel where hydrostatic pressure is balanced by hoop stresses in the vessel walls. Here, mechanical balance appears to define a physical limit to the maximum size MDCK cysts can inflate to based on the plateaus evident at 5h in Fig. 1c, and the early rupture that occurs with overly rapid inflation (e.g. 1.5 mA/mm^2). We hypothesized that these plateaus and rupture can both be linked to cortical cytoskeletal effects in the cysts limiting strain beyond a certain point in a viscoelastic fashion.

Considering the cyst as a simple pressure vessel, we predicted that reducing actomyosin contractility would allow MDCK cysts to inflate to a greater extent due to effectively relaxing the pre-stress in the cyst shell. Using blebbistatin, a myosin inhibitor, and Y-27632, a Rho kinase (ROCK) inhibitor, we inhibited actomyosin contractility of the cysts previous to electrical stimulation. Our data showed that the actomyosin inhibitor treatment successfully disrupted the cortical actomyosin network in MDCK cysts (Fig. 2d) and significantly increased both the inflation rate and the maximum volume that inflated cysts could reach. Both drugs promoted increased inflation, with Blebbistatin treatment showing the strongest effect–up to 1.5-fold higher than positive controls, which is in keeping with data showing blebbistatin, and myosin II inhibition, more effectively softens cellular stiffness relative to ROCK inhibition via Y-compound(56) (Fig. 2e, 2f). In contrast, when we tried to limit inflation by stabilizing actomyosin using jasplakinolide (actin polymerizer) or calyculin A (phosphotase inhibitor), both cases resulted in severe tissue damage upon inflation, suggesting that constraining cytoskeletal rearrangement during active inflation was detrimental to the cyst integrity, perhaps by reducing the maximum allowable strain to failure (Supplementary Videos 7, 8).

These data further show that ion pumping and cytoskeletal mechanics are intimately coupled in facilitating and regulating the electro-inflation response, respectively. To fully capture the biophysical mechanisms behind this phenomenon, we moved towards developing a model in which we couple electrokinetics with established 1D elastic models for pres-

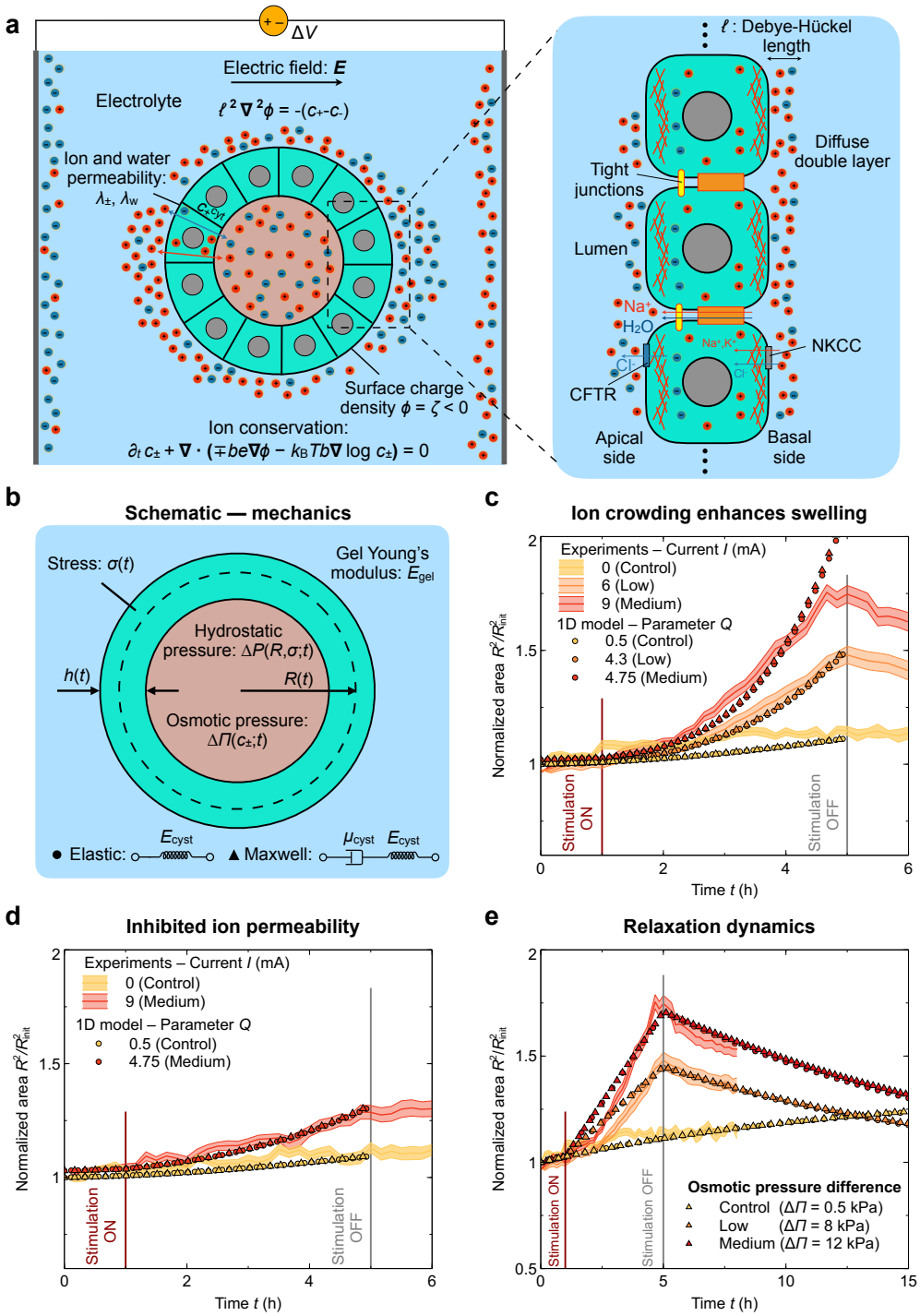

Fig. 3 | Viscoelastic model of MDCK cysts under electrical stimulation recapitulates the inflation dynamics. **a**, Schematic of the 1D and 2D models, in which we consider a spherical MDCK cyst embedded in an electrolyte. An external electric field is applied at $t = 0^+$. The rightmost panel displays a zoom-in schematic of the epithelium showing the different ion and water transport mechanisms considered in the 1D model, as well as a magnified of the electric double cloud of ions surrounding the basal surface of the MDCK cyst (not to scale). **b**, Schematic of the mechanics used in the 1D model, in which we couple hydrostatic pressure ΔP, osmotic pressure $\Delta\Pi$ (which depends on the electrokinetics shown in panel a), gel elasticity, and stress σ of either an elastic (circles) or viscoelastic (triangles) spherical shell of mean radius R and thickness h. **c**-**d**, Normalized area as a function of time obtained from experiments (curves) and 1D model (circles and triangles), for different electric field strengths (see Materials and Methods and Supplementary Information). Panel **d**, corresponds to the knock-out experiment inhibiting ion transport through the epithelium. **e**, Same as in panels c and d but using a simplified 1D model, in which the osmotic pressure increases during stimulation but remains constant over time (see Supplementary Information).

surised epithelial structures.

A mechanical model for MDCK cysts inflation in an electric field. At a bulk level, our data resemble hydraulic pumping into a spherical pressure vessel, which prompted us to develop a 1D continuum model to capture our experimental observations and test our inflation hypotheses *in silico* to help determine the primary driving forces. Here, we considered a minimal model assuming a cyst is either an elastic or a viscoelastic spherical shell embedded in an electrolyte solu-

tion. Initially, we assume the shell behaves as a linearly elastic material and impose cell volume conservation, considering that cells do not proliferate during acute cyst inflation (see Supporting Information text). The main driving mechanism underlying inflation is water transport from the electrolyte into the lumen due to osmotic pressure differences, which is balanced by hydrostatic pressure in our model. Additionally, cyst mechanics, hydrostatic and osmotic pressure, and lumen volume conservation are coupled to the applied electric field via electrokinetic transport of ions around the cyst and across the epithelium (see sketches in Figs. 3a and b). The basic mechanics of this model are well validated in other approaches and contexts involving lumenized structures, which we built on by newly introducing electromechanical coupling to an external electric field (7, 11, 57–65). The full details of our model are thoroughly discussed in our Supporting Information text.

In the control case, with no electric field, the negatively charged basal (outer) surface accumulates a screening layer of counter-ions, usually referred to as the diffuse double layer (DDL) and characterized by its screening thickness referred to as the Debye length (66, 67). Such ion crowding works to neutralize the surface charge but also increases the concentration of ions around the cyst and triggers the transport of species into the lumen due to electro-osmotic effects, as the concentration of ions in the lumen is lower than in the DDL. Moreover, the electric potential across the epithelium also increases due to ion crowding (66, 67), which drives the transport of water across the epithelium via electro-osmosis leading to inflation (60) (Figs. 3c-e, yellow curves).

When an external electric field is applied, the equilibrium state is perturbed and net ion crowding over the basal surface increases, resulting in a thicker DDL and thus a larger Debye length (see Supplementary Information). Such thickening of the DDL triggers increased ion pumping into the lumen, in turn driving enhanced electro-osmotic transport of water and subsequent rapid inflation. Our minimal 1D model recapitulates the inflation dynamics of MDCK cysts both in the absence of an external electric field and during electrical stimulation, as displayed in Fig. 3c. Moreover, our model is also able to capture the MDCK cyst inflation dynamics when ion transport is inhibited (Fig. 3d), as well as the long term relaxation behavior of cysts after stimulation is removed (see Fig. 3e, Supplementary Fig. 10, and Supplementary Information).

These models allowed us to explore different material models; of particular interest given both the rate-dependent rupture shown with the highest current density we tested, and the fact that cysts gradually relaxed back to the volume of unstimulated control cysts after stimulation was removed. Rate dependent material processes can imply viscoelasticity, so we considered the two simplest models to incorporate viscoelasticity at the spherical shell force balance: Maxwell and Kelvin-Voigt materials. A Maxwell material behaves as an elastic solid at times shorter than the so-called Maxwell time, which is the ratio between viscosity and Young's modulus $\mu_{\text{cyst}}/E_{\text{cyst}}$, and exhibits a viscous resistance to deformation at times larger than the Maxwell time (Fig. 3b). A Kelvin-Voigt material behaves oppositely. Here, we find that the Maxwell model was effectively identical to the purely elastic model (Figs. 3c-e), while we were unable to fit a Kelvin-Voigt material to our inflation dynamics (see Supplementary Information). Together, these data suggest that viscous effects take place at time scales longer than the actual inflation event. Additionally, we find that both linear elastic and Maxwell materials coupled to electro-kinetics yield a maximum hydrostatic pressure of 1.2-1.8 kPa, for low and medium stimulation, respectively, consistent with previous measurements (10, 11).

Asymmetrical morphology of electrically stimulated MDCK cysts. In addition to inflation itself, we had also observed pronounced and unexpected asymmetry developing in inflating cysts. Visualizing asymmetry required confocal sectioning, which consistently revealed that the thickness of the hemisphere of the cyst facing the anode ('left' in all of our figures) sometimes thinned over the stimulation period, while the cyst wall on the cathode-facing side slightly thickened (Fig. 4a). The thinning side collapsed down to such an extent that the nuclei, aligned tangent to the surface, bulged out. Conversely, cells on the thicker side appeared to crowd together and elongate like a columnar epithelium, with nuclei orienting perpendicular to the surface.

To quantify asymmetry, we measured apico-basal junction morphology in equatorial slices of several cysts both before stimulation began and at the time of maximal inflation and asymmetry. In order to most generally capture the effect of electric stimulation on cyst morphology, we binned cysts into the left and right hemispheres and measured average junction length before and after stimulation. This revealed that, despite some heterogeneity across samples, junctions on the left (or anode-facing) half of the cyst shortened by approximately 2-fold relative to their initial lengths (Fig. 4b, Supplementary Fig. 11). Pairwise analysis reveals the side-dependant heterogeneity in response; the anode-facing hemisphere of the cyst always thins during stimulation, whereas the cathode-facing hemisphere exhibits a full range of response, from thinning to thickening (Fig. 4b, outlay). For a more detailed analysis, we measured distributions of junction length and orientation as a function of junction angular position before stimulation and at the time of maximal inflation (Supplementary Fig. 12, 13). These analyses show that the uniform distribution of junction orientations before stimulation became biased towards junctions oriented along the field lines when stimulation is turned on. However, in both cases, there is a linear relationship between junction orientation and angular position on the cysts. Junction lengths, which were uniformly distributed before stimulation, become more varied at the time of maximal inflation, and longer junctions become biased to the right (or cathode-facing) half of the cyst.

Such geometric asymmetry strongly suggested that the cyst experienced asymmetric electrical cues, despite being exposed to a uniform field gradient. We hypothesized that this could be do to the geometry of the cyst being large enough to locally disrupt the electric field and ion gradients. To in-

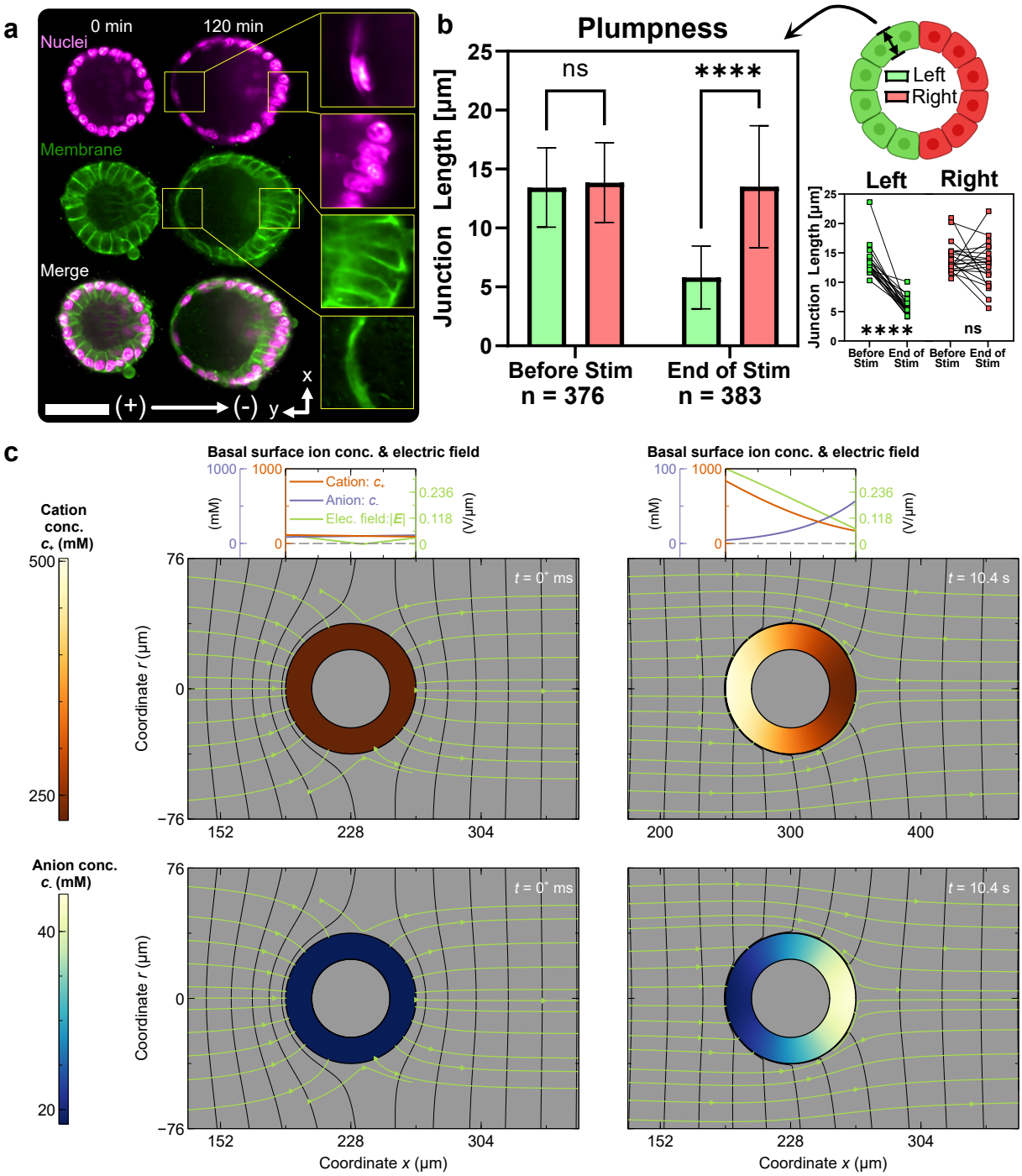

Fig. 4 | Structural asymmetry and ionic stagnation under electrical stimulation. **a**, DC stimulation causes asymmetrical thickening of the cathode-facing half of MDCK cysts. Inlay: Opposing halves of the cyst experience nuclear re-orientation and junctional thinning or thickening. **b**, Junction length averaged over the left and right half of the cyst before and after stimulation (see cartoon). The heterotypic inflation response is captured by the greater error in the right half of the cyst after stimulation ends. Outlay: Pairwise comparisons of averaged junction lengths before and at the end of stim, showing the heterogeneous response. **c**, Color plots displaying 2D axisymmetric electrical potential ϕ isolines (black curves) outside a spherical shell fixed in space representing a lumenized structure, and both cation c_+ (top row) and anion c_- (bottom row) concentrations in the spherical shell at $t = 0^+$ s (left) and $t = 10.4$ s (right). Green curves are electric field streamlines. Top panels show the cation and anion concentration outside at the basal surface at the same times. The directed electric field generates an asymmetric distribution of ions in the epithelium and electric stresses at the basal surface.

vestigate this, we developed a 2D model to recapitulate the ionic micro-environment MDCK cysts experience within a DC field gradient (Fig. 4c). Although our 1D model successfully captured the inflation response dynamics of MDCK cysts under various experimental conditions, DC stimulation necessarily assigns a directionality to our system with cations and anions moving anti-parallel along the field. To fully capture the spatiotemporal ion dynamics in our system, we consider a 2D continuum model building upon previous work on electro-osmotic ion transport (66, 67), motivated by the *in*

vivo relevance of electro-osmotic flow in organ development (68). Rather than reflect long-term mechanical changes, this 2D model was specifically created to capture the transient ionic gradient dynamics that might underlie the asymmetric responses we observe. To do this, we performed numerical simulations taking into account the transport of ion species in an electrolyte solution when an electric field is applied. We assumed that ions permeated the basal surface into the epithelium via basal ion channels, which were modeled considering two average spatially-uniform permeability coefficients for each ion species (60). After permeation, ion diffusion occurs within the cytoplasmic space, which was modeled considering an effective diffusivity (see Materials and Methods).
Our simulations reveal an analog to stagnation point flow in fluids by predicting that cations and anions stagnate over time at the anode-facing and cathode-facing sides of the cyst, respectively (Fig. 4c). In particular, both concentrations increase over time at each side as positive and negative ion species are forced to move towards the cathode and anode respectively, to ensure electroneutrality (Supplementary Video 9). At sufficiently long time, steady state is reached and the tissue shell experiences a highly asymmetric ion distribution as a result of ion stagnation (69, 70), which might drive the morphological asymmetry. One way to investigate this concept was to perturb the electric field dynamics to disrupt this stagnation effect. We performed several experiments to evaluate this. First, we periodically reversed the field polarity at very low frequency (60 min/direction) and observed that the location of the thin membrane switched sides of the cyst to always be on the anode-facing hemisphere (Supplementary Video 10). Second, we used 50 Hz symmetric AC stimulation at our medium current and measured the overall inflation dynamics. We chose this frequency to be on the same timescale as our electrochemical modeling predicted for ion gradient establishment, and we observed that the overall inflation dynamics, while still significantly higher than the control, were dampened compared to DC stimulation and followed a sub-linear trend rather than the exponential trend with DC stimulation (Supplementary Fig. 14). Together, these data demonstrate that: (1) this morphological asymmetry follows the field direction; (2) the asymmetry is reversible; and (3) some level of electrical asymmetry is required to drive a strong inflation response as fast AC stimulation was less effective.

Generality of electrically driven inflation. The ability to electrically control epithelial hydrostatic pressure has exciting implications for developmental biology, biofabrication, and regenerative medicine if it generalizes (10). As our data thus far focused on the MDCK (kidney) model, we next investigated how general the electro-inflation mechanism might be for other lumenized epithelia with more complex cell type populations and architectures. As our key test case, we chose the increasingly popular intestinal organoid model derived from mouse intestinal stem cells. Intestinal organoids are complex, lumenized tissues exhibiting multiple cell types, complex 3D morphologies, and recapitulating key aspects of gut function. Moreover, they represent an entirely distinct organ group relative to our MDCK kidney model, while still being known to exhibit spontaneous, CFTR-mediated inflation and collapse dynamics during cell differentiation and budding morphogenesis, making them a good target model (9, 71). We cultured intestinal organoids using a Matrigel substrate (72) and otherwise identical stimulation conditions to our prior 'medium' stimuli (see Methods).

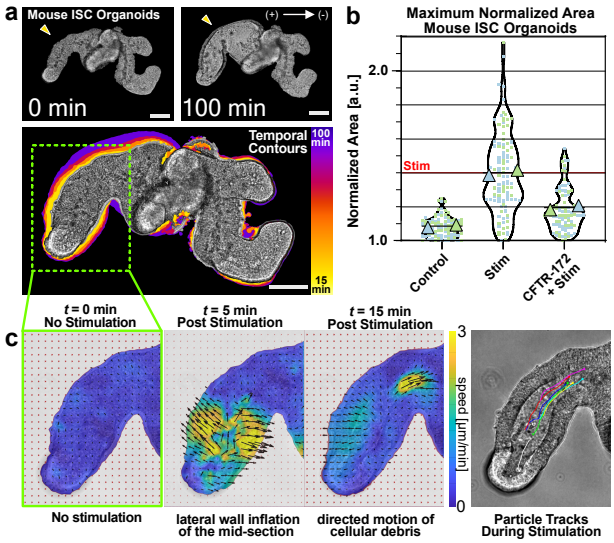

Fig. 5 | Electrical stimulation-induced inflation in mouse ISC organoids. **a**, (Top) Mouse intestinal organoid before ($t = 0$ min) and after ($t = 100$ min) electrical stimulation at medium current. (Bottom) Overlay of outlines for each timepoint. **b**, Maximum normalized area for mouse intestinal organoids with no stimulation, with 2.5 h electrical stimulation at medium current, and with 2.5 h electrical stimulation at medium current with CFTR-172 treatment. **c**, (Panels 1-3) Velocity fields of fluid flow in the lumen of electro-inflating mouse intestinal organoids. (Panel 4) Particle tracks of debris in the lumen of electro-inflating mouse intestinal organoids. All scale bars = 100 μm.

We immediately noticed that intestinal organoids also exhibited electro-inflation, where certain individual lobes inflated quite strongly in many cases (Fig. 5a, Supplementary Video 11, 12). Using the CFTR inhibitor CFTR-172, we proved that CFTR also mediates intestinal organoid electro-inflation, indicating that electrically actuated apical chloride transport may be a general mechanism for the external control of lumenized epithelia and tissue hydrostatic pressure (Fig. 5b). Interestingly, we found significant variability in the response of complex 3D organoid structures, with inflation occurring more often in the main cavity of the organoid compared to the high curvature stem cell crypts, and with instances of directional flow of lumenal debris during electro-inflation (Supplementary Video 11, 12). We investigated this further and used particle-image-velocimetry (PIV) to visualize both the spatiotemporal dynamics of organoid deformation and the emergence of directional flow. These data are shown in Fig. 5c and highlight three things that we also observed in other samples. First, the crypts (high curvature tips of the organoid lobes) exhibit little overall change in cross-section (compare Fig. 5c, $t = 0$ and $t = 5$ min). Second, the majority of the initial deformation seems to occur along the long axis of a lobe (Fig. 5c, t=5 min). Third, there is clear directional flow of debris that emerges during this process, and Fig. 5c at $t = 15$ min shows a fast moving region of debris that is clearly vis-

ible forcing the initial constriction of the lobe open. Particle tracking (Fig. 5c, right) confirmed the majority of debris travel persistently up the lobe, consistent with fluid primarily influxing from the crypt itself. These data emphasize that structural differences in a tissue can contribute to differences in the electro-inflation response, and suggest three hypotheses for future testing. First, crypt cells are known to be mechanically stiffer than the surrounding villi cells, implying crypt zones would deform less under hydrostatic forces (73). Alternately, perhaps there is differential expression of ion channels within different cell types in the organoid, which would alter influx patterns. Finally, and more broadly, the complex 3D geometries might induce ionic 'shadowing' similar to the asymmetric ion distributions described earlier in our 2D model, which might explain the observed heterogeneous response.

Discussion

Our work demonstrates how epithelia are electrically controllable pumps, where external, DC electric fields of physiological magnitudes $\mathcal{O}$(1V/cm) regulate 3D tissue form by controlling water transport. This was unexpected, as our initial assumption was that such uni-directional stimulation would induce classic, migratory electrotaxis in 3D, hollow epithelial spheres. Instead, we found that electrical stimulation induced a tissue-scale phenotype where hollow tissues inflated due to hydrostatic pressure build-up; ultimately caused by cell-level ion pumping and water transport. These findings emphasize both the importance of the bioelectric micro-environment on tissue form and function, and the opportunity to harness this effect to regulate 3D tissue form and function.

We characterized the direct relationship between applied electric field strength and the rate, and extent, of inflation. Broadly, stronger electric field strengths induced faster, more powerful swelling. However, overly strong fields induced premature rupture due to rapid inflation. The inflation process itself is clearly linked to external electric fields triggering CFTR-mediated chloride ion transport, concomitant sodium transport to screen the chloride, and subsequent water transport into the lumen of the tissues to balance the osmotic gradient, causing net inflation. As with several other lumenal tissues (8, 9, 45), CFTR appears to be the primary regulator here, accounting for nearly 2/3 of the total electro-inflation response (Fig. 2b). The net build-up in hydrostatic pressure has mechanical consequences and inflation is constrained by cytoskeletal components. In particular, relaxing acto-myosin contractility significantly enhanced inflation (Fig. 2e) indicating the reinforcing and constraining role of the cytoskeleton on inflation. This cytoskeletal role, along with the rate-dependent rupture during rapid inflation suggest a viscoelastic component that deserves further study.

That electro-inflation can break symmetry and cause dramatic thinning of the anode-facing epithelial wall–was quite surprising and emphasizes how the electrical micro-environment can regulate tissue shape as well as size, perhaps even serving as a symmetry breaking cue *in vivo*. One hypothesis for this is that the different ionic species that may stagnate on either side of a spherical cyst (as suggested by our 2D model in Fig. 4c) might induce separate cellular processes on either side of the cyst. It is possible that these local gradients may alter cytoskeletal activity or pumping dynamics. Such 'ionic shadowing' might also explain why the intestinal organoids exhibited heterogeneous inflation responses in different parts of the complex 3D structures–the intricate geometries might have created a number of local ionic gradients. Alternately, while we do not obviously observe canonical electrotaxis–directed migration typically from anode to cathode–in our tissue spheres, the observed asymmetry pattern could be explained by cells attempting to electrotax on the surface of the cyst, which would lead to cell compression (and the nuclear re-orientation we observe, Fig. 4a) on the cathode-facing side and tension (thinning) on the anode-facing side. Finally, it is possible that emergent differences in mechanical properties of cells in different parts of 3D structures could contribute to asymmetric mechanical reinforcement, and such differences could arise as a secondary response to the prior mechanisms. Interestingly, there is a precedent for both of these mechanobiological hypotheses–migration or stiffening–from Kupffer's vesicle, the organ of asymmetry in zebrafish. This is a lumenized structure that also expresses CFTR and develops a similar asymmetry in wall thickness as cells pack more tightly on the anterior pole in response to differential cortical tension triggered by cilia-transduced shear flow in the lumen (74). Furthermore, these explanations would also be parsimonious with the spatial heterogeneity in our intestinal organoid responses, as there are known differences in the mechanical properties of cell types within intestinal organoids (e.g. Paneth cells are stiffer than stem cells (75), and inflation might induce greater strain in softer cells. Whatever the case, it is clear that the electro-micro-environment could be a source of symmetry breaking and certainly deserves further study.

That environmental electric fields can alter morphogenetic processes raises intriguing possibilities for developmental biology and engineering, especially as water transport and tissue pressure are now known to contribute to development of vasculature, lumenized organs, and embryonic form by modulating cell proliferation, mechanics, and fate(8, 11, 41, 76). The sheer speed of electro-inflation allows much faster perturbation and control than traditional pharmacological agents. Similarly, the speed, throughput, and relatively inexpensive infrastructure compliment delicate mechanical methods (e.g. micro-pipette aspiration and AFM). Further, these benefits play out in a fully 3D context without requiring dimension reduction to 2D, allowing arbitrary 3D tissue structures to be perturbed. Future work to more precisely localize field stimulation could significantly enhance the level of precision here as well.

If we think of electro-inflation as an actuation process, then the epithelium becomes an incredible material–a living, conformal surface with controllable fluid pumping and a number of interesting bioengineering applications are worth exploring, such as in bio-soft robotics (7, 77–79). Here, hydraulic actuation offers an unexpected and potentially useful alterna-

tive to traditional muscle-based actuators. Such engineering applications require a design framework, so it is promising that our preliminary computational models successfully capture and predict the key responses because this could help with formal design and optimization efforts. Overall, it is exciting to consider new uses of bioelectric control of multicellular systems in areas spanning electrochemistry, biosensing, and even water purification (80).

Materials and Methods

Cell Maintenance and Culture. MDCK-II wild type canine kidney cells and RFP E-Cadherin MDCK-II cells (courtesy of the Nelson Lab, Stanford University) were cultured in low-glucose (1 g/L) DMEM with phenol red (Gibco, USA; powder stock), 1 g/L sodium bicarbonate, 1% streptomycin/penicillin (Gibco, USA), and 10% fetal bovine serum (Atlanta Biological, USA)–DMEM++. Cells were incubated at 37°C and 5% CO2 in humidified air. Mouse intestinal stem cell (ISC) organoids were isolated and harvested from HaloYAP-positive mice (courtesy of the Posfai Laboratory, Princeton University) and maintained in culture using reagents and protocol from the IntestiCult OGM Mouse Kit (Stemcell Technologies, Vancouver, Canada).

MDCK Cyst Culture. To ensure that the hydrogel containing MDCK cysts and ISC organoids were within the stimulation zone and to control their shapes and sizes, a silicone stencil of 250 μm thickness (Bisco HT-6240, Stockwell Elastomers) containing two 7.5 x 10mm square microwells was cut and applied to the center of the glass culture substrate using a razor writer (Cameo, Silhouette, Inc.). MDCK-II wild type cells were suspended in a DMEM++ solution of 2.5e5 cells/mL using a Cytosmart Cell Counter for counting. Gibco Geltrex LDEV-Free Reduced Growth Factor Basement Membrane Matrix (Fisher Scientific) was diluted to a 1:1 ratio with DMEM. A first layer of Geltrex/DMEM++ solution of 15μL was deposited onto each 7.5x10 mm2 rectangular stencil , then allowed to solidify for 30 min at 37C. 12.5uL of Geltrex/cell + DMEM++ solution was deposited on top of the first layer, then allowed to solidify for 1 h before the gel was covered with DMEM++ for 96h. Organoids were resuspended into a Corning® Matrigel® Growth Factor Reduced (GFR) Basement Membrane Matrix, Phenol Red-free, LDEV-free, 10 mL (Corning) at a 1:1 ratio with organoid growth medium. 27.5μL of the mixture was deposited onto each of the rectangular stencil and allowed to solidify for 15 min at 37C before the gel was covered with organoid growth medium for 72h.

MDCK Dome Culture. MDCK-II cells were seeded onto tissue-culture plastic surfaces at 4e6 cells/mL density. The tissue culture plastic substrate was first treated with collagen IV dissolved to 50 μg/mL in DI water, which was applied to the dish for 30 min at 37°C, then washed three times with DI water to provide a matrix for cellular adhesion. With the two 7.5 x 10mm square microwell stencil in place, seeding solution of cells was prepared at a density of 2.5 × 10e6 cells, counted using a Cytosmart Cell Counter (Corning) and 10 μL of the cell solution was pipetted into the stencils. The cells were allowed to settle for 1 h with extra humidification media was added to the periphery of the tissue culture dish. Once the cells had adhered to the substrate, sufficient media was added to fill the dish. The stencils were removed 48 h after incubation for assembly.

Live Dead assay. Cyst cultures were treated with 1μM EthD-1 solution (LIVE/DEAD Viability/Cytotoxicity Kit, Invitrogen) for 1 h before electrical stimulation. Identical concentration of EthD-1 was supplemented in the perfusion media to prevent the reagent from washing out during stimulation.

Inhibitor Assays. For actomyosin inhibition, blebbistatin (Selleck Chemical) and Y-27632 (Selleck Chemical) were used at 100μM concentration and added 1h before stimulation. For CFTR channel inhibition, CFTR-172 (Cayman) was used at 50μM and 100μM concentration and added 24h before stimulation for MDCK cysts and 48h before stimulation for ISC organoids. For NKCC inhibition, bumetanide was used at 100μM concentration and added 1h before stimulation. Inhibitors were applied after the patterning stencils were removed to prevent the inhibitors from being absorbed into the PDMS. Identical concentration of inhibitors was supplemented in the perfusion media to prevent the inhibitors from washing out during stimulation.

Electrical stimulation. The uniaxial stimulation device is a modified version of the SCHEEPDOG bioreactor with similar methods from our previous work (29, 30, 34). A Keithley source meter (Kiethly 2450 Textronix) provided current to the silver and silver chloride electrode pair while a USB oscilloscope (Analog Discovery 2, Digilent Inc.) measured the voltage across a pair of recording electrodes (titanium wire, 0.5 mm diameter, Alfa Aesar) as probes. A custom MATLAB script was written to maintain a constant current density within the microfluidic chamber. Samples were imaged for 1h without any electrical stimulation, 4h with the designated electrical field, then 3h without electrical stimulation. A current density of 0.7mA/mm2 corresponds to a field strength of 1V/cm, 1.1mA/mm2 to 2.25V/cm, and 1.5mA/mm2 to 3.5V/cm.

Timelapse Microscopy. Phase contrast images were acquired on an automated inverted microscope (Zeiss Observer Z1; 3i Marianas System) equipped with an XY motorized stage, Photometrics Prime sCMOS, and Slidebook capture software (Intelligent Imaging Innovations, 3i). The microscope was fully incubated at 37°C, and 5% CO2 was constantly bubbled into media reservoir during perfusion. Imaging for MDCK cysts was performed using a Zeiss 10X/0.30 Plan-Neofluor objective and images were captured every 10 minutes at 100ms exposure. Imaging for ISC organoids was performed using a Zeiss 20X/0.80 Plan-Apochromat objective and images were captured every 1 minutes at 100ms exposure. Additional imaging of organoids was performed on

an incubated Nikon Ti2 with a Qi2 CMOS camera and NIS Elements software.
Confocal microscopy was performed at the Princeton University Molecular Biology Confocal Imaging Core using a Nikon Ti2 inverted microscope with a Yokogawa W1 spinning disk and SoRa module. Laser lines 405nm, 488nm, and 561nm were used for DAPI, memGlow, and Ecadherin-RFP markers, respectively. 3μm thick optical slices were captured at 200ms exposure with 15% laser power on all channels. Images were captured using a 40x/1.25 silicone oil immersion objective with a Hamamatsu BT Fusion sCMOS (6.5 μm/px) every 10 minutes. The stage was incubated at 37°C and 5% CO2 was constantly bubbled into media reservoir during perfusion.

Fluorescence staining. For nuclear staining, Hoescht 33342 10mg/mL solution (Invitrogen) was diluted to 1:1000. For membrane staining, Membrane dye (Memglow 488, Cytoskeleton Inc.) was diluted to 100 μM concentration. Both dyes were diluted in serum-free media and added to samples 30 min previous to imaging. For fluorescence actin imaging, MDCK cysts embedded in Geltrex/DMEM++ mixture was fixed using 2% glutaraldehyde solution for 15 minutes and washed twice in PBS. The cells were then permeabilized with 0.1% Triton X-100 (Sigma Aldrich) solution in PBS for 10 minutes. The cells were washed with PBS-Triton solution twice, then incubated with 1% Bovine Serum Albumin solution (Thermo Fisher) for 15 minutes for blocking. Phalloidin (Alexa 488) was diluted to 1:500 in PBS was added and incubated for 1h, then samples were washed and submerged in PBS for imaging.

Inflation Quantification. Briefly, ImageJ/FIJI software (https://imagej.net/software/fiji) was used to find the mid-plane of cysts and binarize the images for further analyses. First, the "find focused slices" plug-in was used to find the mid-plane of each cyst within the z-stack. Once all focused slices within the timelapse were found, images underwent a series of morphological functions including "Enhance Contrast", "Subtract Background', 'Find Edges', and "Gaussian Blur" before thresholding and converting the image to a mask using "Convert to Mask". In order to fill any breaks across the boundary of the mask as well as fill holes within the interior of the mask, the image was dilated three times before running "Fill Holes", after which the image was eroded three times. Finally, "Analyze Particles" was used to remove all but the largest object in the image. Binarized masks were imported to MATLAB (Mathworks, 2020b) for quantification, where the regionprops() function was used to calculate the area of each mask over time. These area dynamics are then normalized by the initial area and filtered by their maximal area and rate of inflation to remove cysts that do not inflate. Inflation dynamics are then averaged together within different experimental conditions (stimulation strength, inhibitor, control, etc.).

Power Law Fitting and Rescaling. To calculate the rescaling factor of the individual Normalized Area (NA) curves, we defined a time τ at which $\mathrm{NA}(\tau) = \alpha$, where α was chosen to be an arbitrary normalized area. This calculation was repeated for several different choices of α, all yielding the same collapse. After calculating τ for each experimental condition (current density, j), $\tau(j)$ was plotted in log-log and fitted to $\tau \propto j^{\mu}$ using linear regression. Finally, the time vector for each individual curve was rescaled as $\Delta t = t/j^{\mu}$.

Junction length quantification. Cell junction lengths in the cysts were measured manually using the built-in MATLAB function ginput(). Equatorial confocal slices of the cyst at the beginning and end of stimulation were loaded into MATLAB and opened into a GUI, wherein the user defines the center of the cyst before sequentially selecting the apical and basal ends of each junction in an arbitrary order. Once the endpoints of each junction are saved, a simple script calculates the junction length, orientation, and angular position within the cyst. Junction metrics are then binned by position for plotting.

Organoid dynamics. Organoid projections were created by z-projecting a time-series as a 'sum' projection in FIJI and then switching to the 'Fire' look-up-table. Particle-Image-Velocimetry was performed using PIVLab 2.56 in MATLAB (81). First, image sequences were registered and masked in FIJI and then imported in PIVLab. 2-pass FFT deformation analysis was used with 64/32 pixels for the passes with a 50 percent step-over and scaling performed within PIVLab. To better capture the directed particle flow, we averaged 3 frames (3 minutes) of PIV vector fields to reduce random background noise. Manual tracking in FIJI allowed us to generate trajectories of dead cells and debris within the organoid.

Supplementary information

All theoretical modeling is discussed in the additional supplementary file. Please refer to Journal-level guidance for any specific requirements.

Data Availability

All study data are included in the article and/or SI Appendix. Microscopy images and data used to generate figures have been deposited in Zenodo (10.5281/zenodo.7348438).

Code Availability

Custom codes for image analysis and numerical simulations can be found on GitHub (github.com/CohenLabPrinceton/CystSwelling). Further code is available from the corresponding authors upon reasonable request.

Author contribution

G.S. and D.J.C. conceived the project. G.S., I.B.B., and D.J.C. designed the research. G.S. and I.B.B. performed

the experiments. I.B.B. and A.M.-C. performed the theoretical calculations. A.M.-C. performed the numerical simulations. G.S., I.B.B., and D.J.C. performed the image analysis. G.S., I.B.B., A.M.-C., and D.J.C. wrote and edited the manuscript/prepared the figures.

Competing interests

The authors declare no competing interests.

ACKNOWLEDGEMENTS
D.J.C. and the project overall were supported by an NIH MIRA Award (R35-GM133574) and an NSF CAREER Award (2046977). G.S. was supported by a Harari Fellowship. I.B.B. was supported by an NSF GRFP Fellowship. A.M.-C. acknowledges support from the Princeton Center for Theoretical Science and the Human Frontier Science Program through the grant LT000035/2021-C. It is a pleasure to acknowledge enlightening discussions with Profs. Howard A. Stone (Princeton University), and Sean Sun (Johns Hopkins University).

Bibliography

1. Sally P Leys and Ana Riesgo. Epithelia, an evolutionary novelty of metazoans. *Journal of Experimental Zoology Part B: Molecular and Developmental Evolution*, 318(6):438–447, 2012.
2. Lucy Erin O'Brien, Mirjam MP Zegers, and Keith E Mostov. Building epithelial architecture: insights from three-dimensional culture models. *Nature reviews Molecular cell biology*, 3(7): 531–537, 2002.
3. Ian G Macara, Richard Guyer, Graham Richardson, Yongliang Huo, and Syed M Ahmed. Epithelial homeostasis. *Current biology*, 24(17):R815–R825, 2014.
4. SJ Mason, AM Paradiso, and RC Boucher. Regulation of transepithelial ion transport and intracellular calcium by extracellular atp in human normal and cystic fibrosis airway epithelium. *British journal of pharmacology*, 103(3):1649–1656, 1991.
5. Vicky Garcia-Hernandez, Miguel Quiros, and Asma Nusrat. Intestinal epithelial claudins: expression and regulation in homeostasis and inflammation. *Annals of the New York Academy of Sciences*, 1397(1):66–79, 2017.
6. I Sabolić and D Brown. Water transport in renal tubules is mediated by aquaporins. *The clinical investigator*, 72(9):698–700, 1994.
7. M. I. Choudhury, M. A. Benson, and S. X. Sun. Trans-epithelial fluid flow and mechanics of epithelial morphogenesis. *Semin. Cell Dev. Biol.*, 131:146–159, 2022. ISSN 1084-9521. doi: https://doi.org/10.1016/j.semcdb.2022.05.020. Special issue: Human embryogenesis by Naomi Moris and Marta Shahbazi / Special Issue: Luminogenesis and Hydraulics in Development by Chii Jou Chan.
8. Naren P Tallapragada, Hailey M Cambra, Tomas Wald, Samantha Keough Jalbert, Diana M Abraham, Ophir D Klein, and Allon M Klein. Inflation-collapse dynamics drive patterning and morphogenesis in intestinal organoids. *Cell Stem Cell*, 28(9):1516–1532, 2021.
9. V. Narayanan, L.E. Schappell, C.R. Mayer, A.A. Duke, T.J. Armiger, P.T. Arsenovic, A. Mohan, K.N. Dahl, J.P. Gleghorn, and D.E. Conway. Osmotic gradients in epithelial acini increase mechanical tension across e-cadherin, drive morphogenesis, and maintain homeostasis. *Curr. Biol.*, 30(4):624–633, 2020.
10. C. J Chan and Takashi Hiiragi. Integration of luminal pressure and signalling in tissue self-organization. *Development*, 147(5):dev181297, 2020.
11. Chii Jou Chan, Maria Costanzo, Teresa Ruiz-Herrero, Gregor Mönke, Ryan J Petrie, Martin Bergert, Alba Diz-Munoz, L Mahadevan, and Takashi Hiiragi. Hydraulic control of mammalian embryo size and cell fate. *Nature*, 571(7763):112–116, 2019.
12. Carlo Matteucci. *Traité des phénomènes électro-physiologiques des animaux*. Fortin, Masson, 1844.
13. Emil Du Bois-Reymond. *Untersuchungen über thierische Elektricität*, volume 2. G. reimer, 1849.
14. Colin D McCaig, Ann M Rajnicek, Bing Song, and Min Zhao. Controlling cell behavior electrically: current views and future potential. *Physiological reviews*, 2005.
15. Greg M Allen, Alex Mogilner, and Julie A Theriot. Electrophoresis of cellular membrane components creates the directional cue guiding keratocyte galvanotaxis. *Current Biology*, 23(7):560–568, 2013.
16. Min Zhao, Bing Song, Jin Pu, Teiji Wada, Brian Reid, Guangping Tai, Fei Wang, Aihua Guo, Petr Walczysko, Yu Gu, et al. Electrical signals control wound healing through phosphatidylinositol-3-oh kinase-γ and pten. *Nature*, 442(7101):457–460, 2006.
17. Yunyun Shen, Trisha Pfluger, Fernando Ferreira, Jiebing Liang, Manuel F Navedo, Qunli Zeng, Brian Reid, and Min Zhao. Diabetic cornea wounds produce significantly weaker electric signals that may contribute to impaired healing. *Scientific reports*, 6(1):1–12, 2016.
18. Elias H Barriga, Kristian Franze, Guillaume Charras, and Roberto Mayor. Tissue stiffening coordinates morphogenesis by triggering collective cell migration in vivo. *Nature*, 554(7693): 523–527, 2018.
19. Colin D McCaig, Bing Song, and Ann M Rajnicek. Electrical dimensions in cell science. *Journal of cell science*, 122(23):4267–4276, 2009.
20. Barbara Cortese, Ilaria Elena Palamà, Stefania D'Amone, and Giuseppe Gigli. Influence of electrotaxis on cell behaviour. *Integrative Biology*, 6(9):817–830, 2014.
21. Michael Levin, Giovanni Pezzulo, and Joshua M Finkelstein. Endogenous bioelectric signaling networks: exploiting voltage gradients for control of growth and form. *Annual review of biomedical engineering*, 19:353–387, 2017.
22. Peter Friedl and Darren Gilmour. Collective cell migration in morphogenesis, regeneration and cancer. *Nature reviews Molecular cell biology*, 10(7):445–457, 2009.
23. Bo-jian Lin, Shun-hao Tsao, Alex Chen, Shu-Kai Hu, Ling Chao, and Pen-hsiu Grace Chao. Lipid rafts sense and direct electric field-induced migration. *Proceedings of the National Academy of Sciences*, 114(32):8568–8573, 2017.
24. A. Sarkar, B. M. Kobylkevich, D. M. Graham, and M. A. Messerli. Electromigration of cell surface macromolecules in dc electric fields during cell polarization and galvanotaxis. *J. Theor. Biol.*, 478:58–73, 2019.
25. Thuan Beng Saw, Xumei Gao, Muchun Li, Jianan He, Anh Phuong Le, Supatra Marsh, Keng-hui Lin, Alexander Ludwig, Jacques Prost, and Chwee Teck Lim. Transepithelial potential difference governs epithelial homeostasis by electromechanics. *Nature Physics*, 18 (9):1122–1128, 2022.
26. Johnathan G Lyon, Sheridan L Carroll, Nassir Mokarram, and Ravi V Bellamkonda. Electrotaxis of glioblastoma and medulloblastoma spheroidal aggregates. *Scientific reports*, 9 (1):1–19, 2019.
27. Brian Reid and Min Zhao. The electrical response to injury: molecular mechanisms and wound healing. *Advances in wound care*, 3(2):184–201, 2014.
28. Daniel J Cohen, W James Nelson, and Michel M Maharbiz. Galvanotactic control of collective cell migration in epithelial monolayers. *Nature materials*, 13(4):409–417, 2014.
29. Gawoon Shim, Danelle Devenport, and Daniel J Cohen. Overriding native cell coordination enhances external programming of collective cell migration. *Proceedings of the National Academy of Sciences*, 118(29):e2101352118, 2021.
30. Abraham E Wolf, Matthew A Heinrich, Isaac B Breinyn, Tom J Zajdel, and Daniel J Cohen. Short-term bioelectric stimulation of collective cell migration in tissues reprograms long-term supracellular dynamics. *PNAS nexus*, 1(1):pgac002, 2022.
31. Youngbin Cho, Minjeong Son, Ung Hyun Ko, Hyuntae Jeong, and Jennifer Hyunjong Shin. Electric stimulation alters intercellular stress within the epithelial monolayer. *The FASEB Journal*, 32:869–3, 2018.
32. Yashar Bashirzadeh, Jonathan Poole, Shizhi Qian, and Venkat Maruthamuthu. Effect of pharmacological modulation of actin and myosin on collective cell electrotaxis. *Bioelectromagnetics*, 39(4):289–298, 2018.
33. Li Li, Robert Hartley, Bjoern Reiss, Yaohui Sun, Jin Pu, Dan Wu, Francis Lin, Trung Hoang, Soichiro Yamada, Jianxin Jiang, et al. E-cadherin plays an essential role in collective directional migration of large epithelial sheets. *Cellular and Molecular Life Sciences*, 69(16): 2779–2789, 2012.
34. Tom J Zajdel, Gawoon Shim, Linus Wang, Alejandro Rossello-Martinez, and Daniel J Cohen. Scheepdog: programming electric cues to dynamically herd large-scale cell migration. *Cell systems*, 10(6):506–514, 2020.
35. Tom J Zajdel, Gawoon Shim, and Daniel J Cohen. Come together: On-chip bioelectric wound closure. *Biosensors and Bioelectronics*, 192:113479, 2021.
36. Claudia G. Vasquez, Vipul T. Vachharajani, Carlos Garzon-Coral, and Alexander R. Dunn. Physical basis for the determination of lumen shape in a simple epithelium. *Nature Communications*, 12(1):1–12, 2021. ISSN 20411723. doi: 10.1038/s41467-021-25050-3.
37. Zhiqiang Zhao, Kan Zhu, Yan Li, Zijie Zhu, Linjie Pan, Tingrui Pan, Richard B Borgens, and Min Zhao. Optimization of electrical stimulation for safe and effective guidance of human cells. *Bioelectricity*, 2(4):372–381, 2020.
38. Qi Bao and R Colin Hughes. Galectin-3 and polarized growth within collagen gels of wild-type and ricin-resistant mdck renal epithelial cells. *Glycobiology*, 9(5):489–495, 1999.
39. Elan Gin, Elly M Tanaka, and Lutz Brusch. A model for cyst lumen expansion and size regulation via fluid secretion. *Journal of theoretical biology*, 264(3):1077–1088, 2010.
40. Adam Navis, Lindsay Marjoram, and Michel Bagnat. Cftr controls lumen expansion and function of kupffer's vesicle in zebrafish. *Development*, 140(8):1703–1712, 2013.
41. Adam Navis and Michel Bagnat. Developing pressures: fluid forces driving morphogenesis. *Current opinion in genetics & development*, 32:24–30, 2015.
42. SM Wilson, RE Olver, and DV Walters. Developmental regulation of lumenal lung fluid and electrolyte transport. *Respiratory physiology & neurobiology*, 159(3):247–255, 2007.
43. Jaroslav Ferenc, Panagiotis Papasaikas, Jacqueline Ferralli, Yukio Nakamura, Sebastien Smallwood, and Charisios D Tsiairis. Mechanical oscillations orchestrate axial patterning through wnt activation in hydra. *Science Advances*, 7(50):eabj6897, 2021.
44. Hongyu Li, Iain A Findlay, and David N Sheppard. The relationship between cell proliferation, cl- secretion, and renal cyst growth: a study using cftr inhibitors. *Kidney international*, 66(5):1926–1938, 2004.
45. CM Haws, IB Nepomuceno, ME Krouse, H Wakelee, T Law, Y Xia, H Nguyen, and JJ Wine. Delta f508-cftr channels: kinetics, activation by forskolin, and potentiation by xanthines. *American Journal of Physiology-Cell Physiology*, 270(5):C1544–C1555, 1996.
46. Roberto Mangoo-Karim, Marie Uchic, Claude Lechene, and Jared J Grantham. Renal epithelial cyst formation and enlargement in vitro: dependence on camp. *Proceedings of the National Academy of Sciences*, 86(15):6007–6011, 1989.
47. Baoxue Yang, Nitin D Sonawane, Dan Zhao, Stefan Somlo, and AS2440296 Verkman. Small-molecule cftr inhibitors slow cyst growth in polycystic kidney disease. *Journal of the american society of nephrology*, 19(7):1300–1310, 2008.
48. Kai Xiao, Lei Jiang, and Markus Antonietti. Ion transport in nanofluidic devices for energy harvesting. *Joule*, 3(10):2364–2380, 2019.
49. Raymond A Frizzell and John W Hanrahan. Physiology of epithelial chloride and fluid secretion. *Cold Spring Harbor perspectives in medicine*, 2(6):a009563, 2012.
50. Vinciane Saint-Criq and Michael A Gray. Role of cftr in epithelial physiology. *Cellular and Molecular Life Sciences*, 74(1):93–115, 2017.
51. Rita Rosenthal, Susanne Milatz, Susanne M Krug, Beibei Oelrich, Jörg-Dieter Schulzke, Salah Amasheh, Dorothee Günzel, and Michael Fromm. Claudin-2, a component of the tight junction, forms a paracellular water channel. *Journal of cell science*, 123(11):1913–1921, 2010.
52. Tonghui Ma, Jay R Thiagarajah, Hong Yang, Nitin D Sonawane, Chiara Folli, Luis JV Galietta, AS151633 Verkman, et al. Thiazolidinone cftr inhibitor identified by high-throughput screening blocks cholera toxin–induced intestinal fluid secretion. *The Journal of clinical investigation*, 110(11):1651–1658, 2002.
53. N Melis, M Tauc, M Cougnon, S Bendahhou, S Giuliano, I Rubera, and C Duranton. Revisiting cftr inhibition: a comparative study of cftr inh-172 and glyh-101 inhibitors. *British journal of pharmacology*, 171(15):3716–3727, 2014.

54. Samuel J Lord, Katrina B Velle, R Dyche Mullins, and Lillian K Fritz-Laylin. Superplots: Communicating reproducibility and variability in cell biology. *Journal of Cell Biology*, 219(6), 2020.
55. Ernest Latorre, Sohan Kale, Laura Casares, Manuel Gómez-González, Marina Uroz, Léo Valon, Roshna V Nair, Elena Garreta, Nuria Montserrat, Aránzazu Del Campo, et al. Active superelasticity in three-dimensional epithelia of controlled shape. *Nature*, 563(7730):203–208, 2018.
56. Jan Christian Martens and Manfred Radmacher. Softening of the actin cytoskeleton by inhibition of myosin ii. *Pflügers Archiv-European Journal of Physiology*, 456(1):95–100, 2008.
57. Y. Li, Y. Mori, and S. X. Sun. Flow-driven cell migration under external electric fields. *Phys. Rev. Lett.*, 115(26):268101, 2015.
58. Sabyasachi Dasgupta, Kapish Gupta, Yue Zhang, Virgile Viasnoff, and Jacques Prost. Physics of lumen growth. *Proceedings of the National Academy of Sciences of the United States of America*, 115(21):E4751–E4757, 2018. ISSN 10916490. doi: 10.1073/pnas.1722154115.
59. C. Duclut, N. Sarkar, J. Prost, and F. Jülicher. Fluid pumping and active flexoelectricity can promote lumen nucleation in cell assemblies. *Proc. Natl. Acad. Sci. U.S.A.*, 116(39): 19264–19273, 2019.
60. A. Torres-Sánchez, M. K. Winter, and G. Salbreux. Tissue hydraulics: physics of lumen formation and interaction. *Cells Dev.*, 168:203724, 2021.
61. M. Le Verge-Serandour and H. Turlier. Blastocoel morphogenesis: A biophysics perspective. *Semin. Cell Dev. Biol.*, 130:12–23, 2022. ISSN 1084-9521. doi: https://doi.org/10.1016/j.semcdb.2021.10.005. Special issue: The control of tissue size and shape by Yanlan Mao and Franck Pichaud.
62. M. Le Verge-Serandour and H. Turlier. A hydro-osmotic coarsening theory of biological cavity formation. *PLoS Comput. Biol.*, 17(9):e1009333, 2021.
63. C. Duclut, J. Prost, and F. Jülicher. Hydraulic and electric control of cell spheroids. *Proc. Natl. Acad. Sci. U.S.A.*, 118(19):e2021972118, 2021.
64. M. Bagnat, B. Daga, and S. Di Talia. Morphogenetic roles of hydrostatic pressure in animal development. *Annu. Rev. Cell Dev. Biol.*, 38, 2022.
65. M. Popović, J. Prost, and F. Jülicher. Electrohydraulic activity of biological cells. *arXiv preprint arXiv:2211.06909*, -(-):–, 2022.
66. M. Z. Bazant and T. M. Squires. Induced-charge electrokinetic phenomena: theory and microfluidic applications. *Phys. Rev. Lett.*, 92(6):066101, 2004.
67. T. M. Squires and M. Z. Bazant. Induced-charge electro-osmosis. *J. Fluid Mech.*, 509: 217–252, 2004.
68. Paula C Sanematsu, Gonca Erdemci-Tandogan, Himani Patel, Emma M Retzlaff, Jeffrey D Amack, and M Lisa Manning. 3d viscoelastic drag forces contribute to cell shape changes during organogenesis in the zebrafish embryo. *Cells Dev.*, 168:203718, 2021.
69. Roberto Lagunes, Lourdes Ruiz, and Eugenio Frixione. Contraction of epithelial (mdck) cells in response to low extracellular calcium is dependent on extracellular sodium. *Journal of Muscle Research & Cell Motility*, 20(8):761–770, 1999.
70. Eugenio Frixione, Roberto Lagunes, Lourdes Ruiz, Mercedes Urbán, and R Michael Porter. Mechanical responses of single non-confluent epithelial cells to low extracellular calcium. *Journal of Muscle Research & Cell Motility*, 24(7):477–485, 2003.
71. Gerald Schwank, Bon-Kyoung Koo, Valentina Sasselli, Johanna F Dekkers, Inha Heo, Turan Demircan, Nobuo Sasaki, Sander Boymans, Edwin Cuppen, Cornelis K van der Ent, et al. Functional repair of cftr by crispr/cas9 in intestinal stem cell organoids of cystic fibrosis patients. *Cell stem cell*, 13(6):653–658, 2013.
72. Denise Serra, Urs Mayr, Andrea Boni, Ilya Lukonin, Markus Rempfler, Ludivine Challet Meylan, Michael B Stadler, Petr Strnad, Panagiotis Papasaikas, Dario Vischi, et al. Self-organization and symmetry breaking in intestinal organoid development. *Nature*, 569(7754): 66–72, 2019.
73. Wang Xi, Jad Saleh, Ayako Yamada, Caterina Tomba, Barbara Mercier, Sébastien Janel, Tien Dang, Matis Soleilhac, Aurélie Djemat, Huiqiong Wu, et al. Modulation of designer biomimetic matrices for optimized differentiated intestinal epithelial cultures. *Biomaterials*, 282:121380, 2022.
74. Guangliang Wang, M Lisa Manning, and Jeffrey D Amack. Regional cell shape changes control form and function of kupffer's vesicle in the zebrafish embryo. *Developmental biology*, 370(1):52–62, 2012.
75. Alistair J Langlands, Axel A Almet, Paul L Appleton, Ian P Newton, James M Osborne, and Inke S Näthke. Paneth cell-rich regions separated by a cluster of lgr5+ cells initiate crypt fission in the intestinal stem cell niche. *PLoS biology*, 14(6):e1002491, 2016.
76. Allyson Quinn Ryan, Chii Jou Chan, François Graner, and Takashi Hiiragi. Lumen expansion facilitates epiblast-primitive endoderm fate specification during mouse blastocyst formation. *Developmental cell*, 51(6):684–697, 2019.
77. G.M. Whitesides. Soft robotics. *Angew. Chem., Int. Ed. Engl.*, 57(16):4258–4273, 2018.
78. Mingqi Zhang, Guori Li, Xuxu Yang, Youhua Xiao, Tao Yang, Tuck-Whye Wong, and Tiefeng Li. Artificial muscle driven soft hydraulic robot: electromechanical actuation and simplified modeling. *Smart Materials and Structures*, 27(9):095016, 2018.
79. Leonardo Ricotti, Barry Trimmer, Adam W Feinberg, Ritu Raman, Kevin K Parker, Rashid Bashir, Metin Sitti, Sylvain Martel, Paolo Dario, and Arianna Menciassi. Biohybrid actuators for robotics: A review of devices actuated by living cells. *Science robotics*, 2(12):eaaq0495, 2017.
80. Andrew R Koltonow and Jiaxing Huang. Two-dimensional nanofluidics. *Science*, 351(6280): 1395–1396, 2016.
81. William Thielicke and Eize Stamhuis. Pivlab–towards user-friendly, affordable and accurate digital particle image velocimetry in matlab. *Journal of open research software*, 2(1), 2014.